P H Y S I C A L R E V I E W L E T T E R S

Charge Catastrophe and Dielectric Breakdown During Exposure of Organic Thin Films to Low-Energy Electron Radiation

A. Thete,[1,2] D. Geelen,[1] S. J. van der Molen,[1] and R. M. Tromp[1,3]

[1]*Leiden University, Huygens-Kamerlingh Onnes Laboratory, P.O. Box 9504, 2300 RA Leiden, The Netherlands*
[2]*Advanced Research Center for Nanolithography, Science Park 102, 1098 XG Amsterdam, The Netherlands*
[3]*IBM T.J. Watson Research Center, 1101 Kitchawan Road, Yorktown Heights, New York 10598, USA*

The effects of exposure to ionizing radiation are central in many areas of science and technology, including medicine and biology. Absorption of UV and soft-x-ray photons releases photoelectrons, followed by a cascade of lower energy secondary electrons with energies down to 0 eV. While these low energy electrons give rise to most chemical and physical changes, their interactions with soft materials are not well studied or understood. Here, we use a low energy electron microscope to expose thin organic resist films to electrons in the range 0–50 eV, and to analyze the energy distribution of electrons returned to the vacuum. We observe surface charging that depends strongly and nonlinearly on electron energy and electron beam current, abruptly switching sign during exposure. Charging can even be sufficiently severe to induce dielectric breakdown across the film. We provide a simple but comprehensive theoretical description of these phenomena, identifying the presence of a cusp catastrophe to explain the sudden switching phenomena seen in the experiments. Surprisingly, the films undergo changes at *all* incident electron energies, starting at ∼0 eV.

The interaction of ionizing radiation with matter is of vast scientific and technological (including biological and medical) importance. The interaction of UV and x-ray photons with matter is mediated by photoelectrons, as well as secondary electrons with a broad energy distribution that induce chemical changes in the material, be it a polymer, organic or inorganic hybrid, biological tissue, or even DNA. But these complex processes are hard to disentangle, as photon illumination sets the entire electron cascade in motion at once, without the possibility of discerning the role of electrons with different energies. As a result, the interaction of low energy electrons (LEEs) with soft matter is not well understood. Here, we focus primarily on the interaction of low energy electrons with polymethylmethacrylate (PMMA) and related resist materials as used in extreme ultraviolet (EUV) lithography [1] to obtain a new understanding of key processes at low electron energies.

In a low energy electron microscope [2] (LEEM) a sample is illuminated with electrons with adjustable 0–100 eV energy [3]. We use LEEM to expose thin PMMA films, monitoring changes both after and during exposure [4]. The radiation *chemistry* of PMMA and related materials has been well studied, and there is consensus that irradiation causes scission of the main chains and removal of side groups [5–10]. Here, we identify key *physical* processes largely ignored in the literature: resist charging, exposure-induced changes in conductivity and secondary electron emission, and dielectric breakdown. We present a simple quantitative theory describing our data, identifying a cusp catastrophe [11] causing the instabilities seen during exposure. Even

electrons with *near-zero* energy change the resist, suggestive of dissociative electron attachment processes [12] commonly neglected in resist modeling. Our results provide new insights into LEE interactions in a broader sense, deepening our knowledge of the interaction of ionizing radiation with soft matter.

Experiments were performed in the ESCHER LEEM facility [4] at Leiden University. The sample is immersed in an electrostatic field of ∼100 kV/cm, slowing the 15 keV electrons produced by the gun to tunable 0–100 eV incident energy, E_0. Secondary electrons leaving the sample are extracted by this field, and can never return [2–4]. The experiment is schematically shown in Fig. 1(b).

Figure 1(a) shows a 20 nm PMMA film exposed to varying electron energies, currents, and doses [4]. Each bright spot represents a single exposure with ∼5 μm ∅. Between exposures the beam is blanked, and the sample position is advanced. With all exposures complete the sample is developed in 1:3 isopropyl alcohol:methyl isobutyl-ketone for 1 min, and viewed under an optical microscope. We find an apparent energy threshold below which the resist is not exposed. This threshold depends on beam current, increasing from ∼15 eV at 0.05 nA, to ∼18 eV at 2 nA, but not on dose. We will show that this threshold shift is not related *directly* to electron energy, but to charging of the resist, which depends on electron energy and current, electrical conductivity of the resist, and secondary electron emission (SEE). Below threshold the PMMA surface accumulates sufficient negative charge to reflect the incident electrons and prevent them from reaching the sample. Figure 1(c) shows some of the elementary
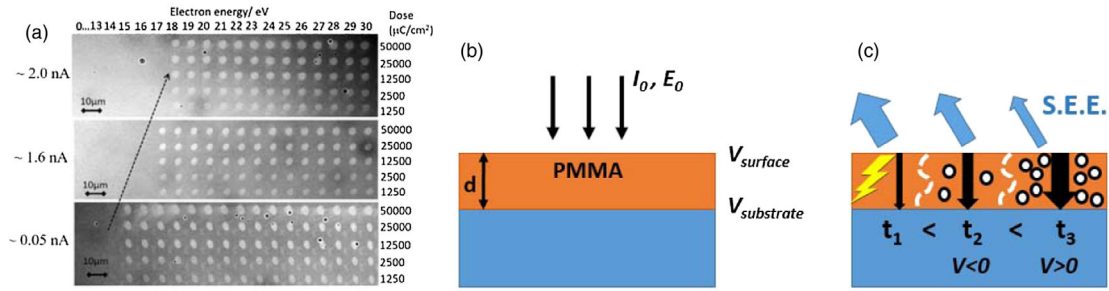
FIG. 1. (a) PMMA exposures as a function of electron current, energy, and dose. At each current (0.05, 1.6, and 2.0 nA) we find an exposure threshold which does not depend on dose. PMMA thickness 20 ± 4 nm, spin-coated onto a Si substrate. (b) An electron beam with current density I_0 impinges on PMMA of thickness d. E_0 is the electron energy relative to $V_{\text{substrate}}$. The surface charges to a potential V_{surface}. The charging voltage V is defined as $V = V_{\text{substrate}} - V_{\text{surface}}$. (c) Schematic of elementary processes, including electrical breakdown (time t_1), increasing trap creation (white dots at t_2 and t_3), decreasing SEE and increasing conductance during exposure, V switching sign between t_2 and t_3. These processes depend on experimental parameters that change over time.

processes, i.e., surface charging, dynamic changes in PMMA conductance and secondary electron emission, and the balance between them. At short times charging can be so severe as to give rise to dielectric breakdown across the PMMA film.

Figures 2(a)–2(e) present energy spectra of electrons reflected and/or emitted by the sample during exposure [13], for E_0 from 14–30 eV (0.25 nA, 5 μm $\varnothing$). Electron intensity is shown vs energy and time. $E_0 \leq 14$ eV [Fig. 2(a)] yields only specularly reflected electrons, implying that the surface charges to the beam energy, and all electrons are backreflected before reaching the sample. At $E_0 = 15$ eV Fig. 2(b) first shows a narrow spectrum, as the electrons are decelerated to near-zero energy by accumulation of negative surface charge. The spectrum width increases over time as negative charge diminishes, thereby increasing the landing energy, E_{land}. In Fig. 2(c), the initial signal at ~31 eV *exceeds* $E_0 = 20$ eV, i.e., the incident electrons are accelerated from 20 to 31 eV due to accumulation of *positive* charge. E_{land} slowly decreases, followed by a sudden drop to ~15 eV. In Figs. 2(d)–2(e) we again find an initial acceleration of the incident electrons, with a drop of E_{land} during the first few seconds to $E_{\text{land}} \approx E_0 + 5$ eV. Then E_{land} slowly decreases, followed again by a sudden drop near the center of the data

sets. Such erratic and unstable behavior cannot be understood in a static picture of electron-PMMA interaction.

To understand the threshold, we define the substrate as one electrode, and the PMMA surface as a second "virtual" electrode on which charge can accumulate, and then flow to the substrate. V is defined as $V_{\text{substrate}} - V_{\text{surface}}$ [Fig. 1(b)]. The current density from surface to substrate is given by the Mott-Gurney law for space-charge-limited conductance [14]:

$$I(V) = \pm g V^2, \tag{1}$$

where $g = 9\varepsilon\mu/8d^3$ (dielectric constant ε, mobility μ, thickness d). The minus sign applies for $V < 0$.

The Gaussian energy distribution of the electron beam is given by

$$I_0(E) = I_0 \frac{1}{\sqrt{2\pi\sigma^2}} e^{-\frac{(E-E_0)^2}{2\sigma^2}}. \tag{2}$$

E_0 is the incident electron energy relative to $V_{\text{substrate}}$, with standard deviation $\sigma = 0.11$ eV in our experiments. If $V = 0$ (no charging), the incident current equals $\int_0^\infty I_0(E)dE$, which for $E_0 > 0.3$ eV equals I_0. However, for typical current densities I_0 the surface charges to an electron-retarding potential V, and only electrons with $E > V$
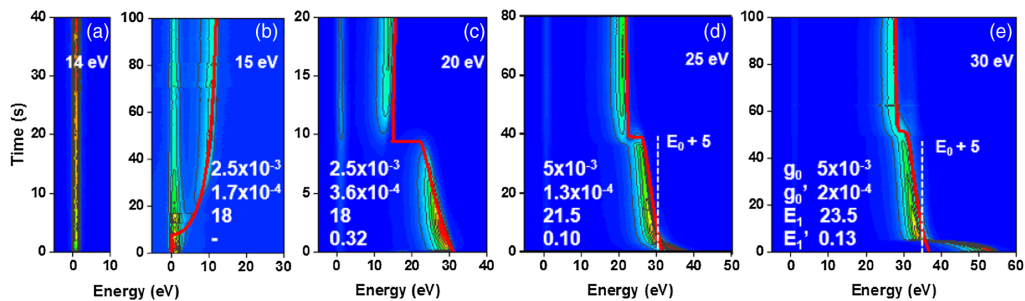

FIG. 2. (a)–(e) Electron energy spectra during exposure for $E_0 = 14, 15, 20, 25,$ and 30 eV. The energy scale is a loss scale, with elastic electrons at zero. Thus, the highest energy at which signal is observed (i.e. the cut-off of the secondary electrons) is a direct measure of E_{land}. In (a) and (e) this corresponds at $t = 0$ to $E_{\text{land}} \approx 0$, and 55 eV, respectively. Red lines are fits based on Eqs. (5), with g_0 and E_1 at $t = 0$, and time derivatives g_0' and E_1' given in the figures.

reach the surface. (We take the electron charge $e = 1$ for convenience.) Then the *net* incident current density is $\int_V^\infty I_0(E)\,dE$. Slower electrons ($E < V$) never reach the sample. In equilibrium the current through the film equals the net incident current:

$$\frac{I(V)}{I_0} = \pm g_0 V^2 = \int\limits_V^\infty \frac{1}{\sqrt{2\pi\sigma^2}} e^{-\frac{(E-E_0)^2}{2\sigma^2}} dE, \qquad (3)$$

where $g_0 = g/I_0$. The PMMA surface charges to a potential V_{eq} that satisfies Eq. (3). Figure 3(a) plots the left-hand side of Eq. (3) vs V for $g_0 = 0.0045$ (black-dashed curve), and the right-hand side (blue lines) for $E_0 = 10$, 15, and 20 eV ($\sigma = 0.11$ eV). Equation (3) is satisfied where the black and blue lines intersect (arrows). For $E_0 = 10$ eV we find $V_{eq} \approx 10$ V (red arrow). About half the electrons reach the sample with near-zero energy, while the other half is reflected back into the vacuum. For $E_0 = 15$ eV, $V_{eq} \approx 14.5$ V (black arrow) and ~95% of the electrons reach the sample with $E_{land} \approx 0.25$ eV. For
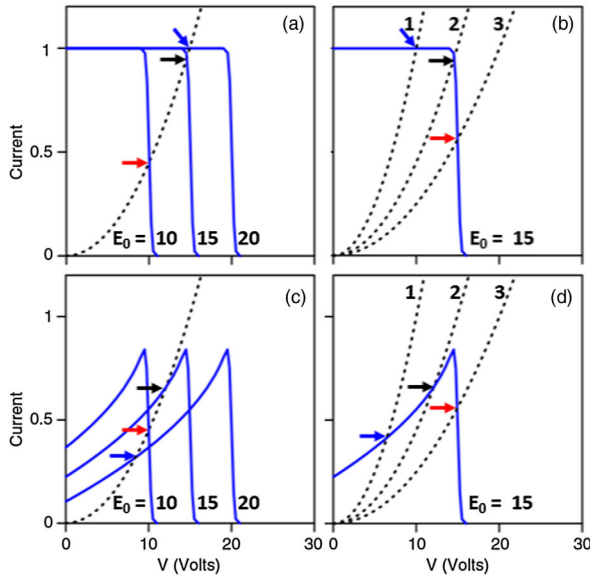

FIG. 3.　(a) Blue lines: Normalized electron current vs V *without* secondary electrons for $E_0 = 10$, 15, and 20 eV. Black dash: left-hand side of Eq. (3) with $g_0 = 0.0045$. Equation (3) is satisfied at the intersections of the blue and black lines (arrows). (b) Blue line: as in (a) with $E_0 = 15$ eV. Black lines: as in (a) with $g_0 = 0.01$ (1), 0.0045 (2), and 0.0025 (3). Charging increases with decreasing g_0, i.e., increasing I_0. (c) Blue lines: Normalized electron current vs V *with* secondary electrons [right-hand side of Eq. 5(b)] for $E_0 = 10$, 15, and 20 eV, $\alpha = 0.5$, and $E_1 = 25$ eV. Black dashed curve: left-hand side of Eq. (3) with $g_0 = 0.0045$. For $E_0 = 10$ eV, V_{eq} has not changed relative to (a), but for $E_0 = 15$ and 20 eV it has decreased markedly (arrows). (d) Blue line: as in (c) with $E_0 = 15$ eV. Black lines: as in (c) with $g_0 = 0.01$ (1), 0.0045 (2), and 0.0025 (3). For the highest beam current (3) V_{eq} has changed little compared to (b). For (1) and (2) V_{eq} has decreased markedly.

$E_0 = 20$ eV, $V_{eq} \approx 14.9$ eV (blue arrow) and all electrons reach the sample with $E_{land} \approx 5.1$ eV. Figure 3(b) plots the right-hand side of Eq. (3) for $E_0 = 15$ eV (blue), and the black-dashed lines are for $g_0 = 0.01$, 0.0045, and 0.0025. Upon decreasing g_0 (increasing I_0), V_{eq} shifts to the right. For the highest I_0 (lowest g_0) the surface charges to E_0 (red arrow), for medium I_0 to just below E_0 (black arrow), and for the lowest I_0 to ~5 V below E_0 (blue arrow). The threshold shifts upwards with I_0, in accordance with Fig. 1(a).

Equation (3) does not account for secondary electrons *leaving* the sample. The SEE coefficient as a function of incident electron energy, $\delta_s(E)$, has been studied extensively [15–23], but is not well characterized below 100 eV. We approximate $\delta_s(E)$ by

$$\delta_s(E) = \left(\frac{E}{E_1}\right)^\alpha. \qquad (4)$$

E_1 is the energy for which $\delta_s(E) = 1$, α falls in the range 0.5–1.5 (the value of α is not critical; see the Supplemental Material [24]).

Secondaries leaving the sample reduce the net electron current reaching the sample; the weight of each incident electron is reduced by $\delta_s(E)$. For incident energy E and charging potential V, $E_{land} = E - V$, and the reduced electron weight is $[1-\delta_s(E_{land})]$, changing Eq. (3) to

$$\frac{I(V)}{I_0} = \pm g_0 V^2 = \int\limits_V^\infty \frac{1}{\sqrt{2\pi\sigma^2}} \left(1 - \left(\frac{E-V}{E_1}\right)^\alpha\right) e^{-\frac{(E-E_0)^2}{2\sigma^2}} dE.$$

$$(5a)$$

Figure 3(c) shows the left-hand side of Eq. (5a) (black-dashed curve, $g_0 = 0.0045$), and the right-hand side for $E_0 = 10$, 15, and 20 eV, taking $E_1 = 25$ eV, $\alpha = 0.5$. Comparison with Fig. 3(a) shows the importance of including SEE: $E_0 = 10$ eV is still well below threshold (red arrow), but $E_0 = 15$ eV is well above (black arrow). For $E_0 = 20$ eV, V_{eq} has shifted from ~15 eV in Fig. 3(a) to ~8 eV in Fig. 3(c) (blue arrow). In Fig. 3(d) we again find this downward shift in V_{eq} (arrows) compared to Fig. 3(b).

If the electron energy distribution is infinitely narrow (δ function), Eq. (5a) simplifies to

$$\frac{I(V)}{I_0} = \pm g_0 V^2 = 1 - \left(\frac{E_0-V}{E_1}\right)^\alpha. \qquad (5b)$$

With $\sigma = 0.11$ eV this excellent approximation is used in the following. Figure 4(a) shows the left-hand side of Eq. (5b) (black-dashed curve, $g_0 = 0.0025$), for $-30 < V < 30$. The blue lines show the right-hand side of Eq. (5b) for $E_0 = 25$ eV, and $E_1 = 20$, 25, and 30 eV, $\alpha = 0.5$. For $E_1 = 30$ eV there is one solution (blue arrow) with $E_0 - V_{eq} = E_{land} < E_0$. For $E_1 = 20$ eV there is one
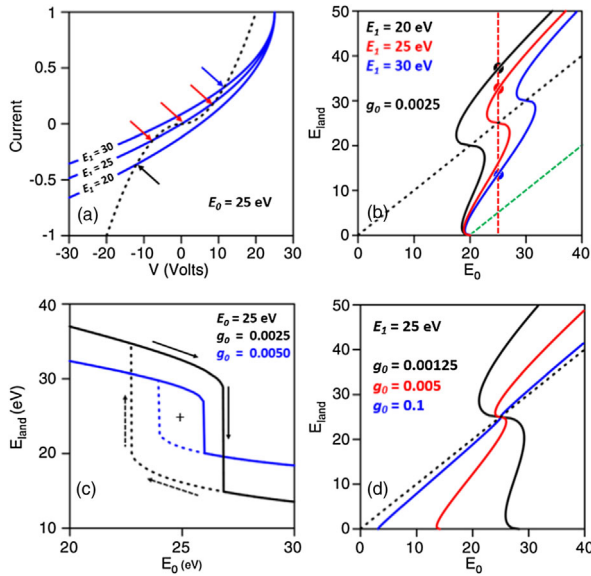
FIG. 4. (a) Black dashed curve: left-hand side of Eq. (5b), $g_0 = 0.0025$. Blue lines: right-hand side of Eq. (5b) for different values of E_1. Arrows indicate solutions of Eq. (5b). (b) Solutions to Eq. (5b) vs E_0 for different values of E_1. $g_0 = 0.0025$. Green dashed line: no secondary electrons (c) E_{land} vs E_1 at $E_0 = 25$ eV. As E_1 increases (solid lines), E_{land} drops abruptly at a critical value. Reducing E_1, the landing energy jumps back up at a much lower value (dashed lines). This hysteresis, characteristic of a cusp catastrophe, closes as g_0 increases (blue lines). (d) Solutions to Eq. (5b) vs E_0 for different values of g_0. $E_1 = 25$ eV. This is typical of a cusp catastrophe with parameters E_0 and g_0. $\alpha = 0.5$ throughout.

solution (black arrow) of opposite sign ($E_{land} > E_0$), corresponding to positive charge accumulation on the surface. Finally, $E_1 = 25$ eV has *three* solutions (red arrows).

Figure 4(b) shows the solutions of Eq. (5b), i.e., $E_{land} = E_0 - V_{eq}$, vs E_0, with $g_0 = 0.0025$ and $E_1 = 20$ (black), 25 (red), and 30 (blue) eV. Again, at $E_0 = 25$ eV (vertical red dash) we find one solution for $E_1 = 20$, and for $E_1 = 30$, and three solutions for $E_1 = 25$ eV. In each case, $E_{land} = 0$ for $E_0 < 20$ eV, i.e., the surface charges to the beam energy, independent of E_1. The curves have an s-shape that depends on E_1, causing the instabilities in Fig. 2 (see below). When there are no secondary electrons ($E_1 \to \infty$) the sample also charges to 20 eV, beyond which E_{land} increases linearly with E_0 (green dash).

Alternatively, we can change g_0 from 0.001 25 [Fig. 4(d), black], to 0.005 (red), and 0.1 (blue). Increasing g_0 corresponds to increasing conductance, or decreasing I_0. For $g_0 = 0.1$ we find a low threshold of ~3 eV, and $E_{land} \cong E_0$. The black dashed line, $E_{land} = E_0$, represents no charging ($g_0 \to \infty$). For lower g_0 the threshold increases, in agreement with Fig. 1(a). The s shapes become more pronounced for lower g_0, i.e., for high resistance and/or high I_0 there is the possibility of multiple values of E_{land} over some range of E_0 centered around E_1. Generically, Figs. 4(b)–4(d) are

emblematic of a so-called cusp catastrophe [11], where one may expect unstable behavior.

Two factors cause the instabilities in Fig. 2: exposure-induced reduction in SEE (increasing E_1), as well as increasing conductance (g_0). First consider SEE, starting with E_{land} on the upper branch of the black s curve in Fig. 4(d) for $E_0 = 25$ eV (black dot), i.e., the only solution available for these initial values. Increasing E_1 from 20 to 25 to 30 eV, the s curves shift to the right from black to red to blue. As the s curve shifts to the right, E_{land} will stay on the upper branch until this ceases to exist at $E_0 = 25$ eV. At that point, E_{land} jumps from the upper (black and red dots) to the lower branch (blue dot). Hence, charging changes sign abruptly upon a continuous shift of E_1 during electron exposure as shown by the solid black line in Fig. 4(c). Going from high to low E_1 [dashed black line, Fig. 4(c)], we meet a second unstable point at lower E_1, forming a hysteresis loop. In Fig. 4(d), the excursions of the s curve are reduced as g_0 increases: the hysteresis loop shrinks as g_0 increases from 0.0025 to 0.005 [Fig. 4(c), blue lines]. Again, this is emblematic of a cusp catastrophe [11]. Of course, the experiment can only move from low to high E_1, as exposure-induced changes are irreversible. Figure 4(c) suggests that increasing E_1 causes the jumps in Fig. 2, while g_0 controls the height of the jumps.

Changes in SEE during electron exposure are well documented: bond breaking leads to creation of traps which capture secondary electrons and reduce SEE (upward shift of E_1) [22]. Similarly, trap creation leads to doping of the PMMA, and increases conductance (and thus g_0) during exposure. Increasing E_1 (i.e., decreasing SEE during exposure) causes the jump in Fig. 4(c), while increasing g_0 reduces the size of the jump.

Returning to Figs. 2(b)–2(e), the red lines are fits using Eq. (5b), linearly increasing g_0 and E_1 with time. In Fig. 2(b) we only change g_0, as the experiment (near threshold) is not very sensitive to E_1. Going from (b) to (e), both g_0 and E_1 increase with exposure. In Figs. 2(b) and 2(c) we start with $g_0 = 0.0025$, $E_1 = 18$ eV, and in Fig. 2(e) we finish the experiment with $g_0 = 0.025$, $E_1 = 36$ eV, i.e., a 10-fold increase in g_0, and a twofold increase in E_1.

In Figs. 2(d)–2(e) we observe a drop in E_{land} during the first few seconds that is not included in the fits. We now introduce a *third* phenomenon, ignored thus far: dielectric breakdown. In Fig. 2(d), the initial E_{land} exceeds 40 eV, i.e., $V_{eq} > 15$ V, corresponding to a field strength > 7.5 MV/cm. In Fig. 2(e), with an initial $V_{eq} > 25$ V, the field strength exceeds 12.5 MV/cm. (These initial landing energies are again consistent with starting values of $g_0 \approx 0.0025$ and $E_1 \approx 18$ eV.) In Fig. 2(c) the initial field strength is ≈ 5 MV/cm, in Fig. 2(b) ~ 7 MV/cm. Thus, the dielectric breakdown strength exceeds 7 MV/cm, a factor 2 larger than previous observations [25]. At higher fields

(and assisted by incident electrons with $E_{land} > 40$ eV), the PMMA films undergo dielectric breakdown, until they become sufficiently conductive to reduce the charging potential, thereby stopping breakdown. In Figs. 2(d)–2(e) the film stabilizes after a few seconds at a charging potential of ∼5 eV, leading to $E_{land} = 30$ and 35 eV, respectively. Now the normal charging and exposure processes take over, and the data are well described by Eq. (5b), as shown by the fits in Figs. 2(d)–2(e).

The rates of change in g_0 and E_1 don't depend strongly on electron energy. In Fig. 2(b) where $E_{land} \approx 0$, g_0 increases only a factor of 2 slower than for $E_{land} \approx 30$ eV [Fig. 2(c)]. In Figs. 2(d)–2(e) the rates are somewhat smaller, after the initial breakdown-induced changes.

With some of the basic processes already previewed in Fig. 1(c), our analysis reveals a wealth of information: (i) During electron exposure the PMMA surface charges due to limited conductance. (ii) Charging can be either positive or negative, with a change in sign when $E_0 \approx E_1$ [Fig. 4(c)]. The initial value of $E_1 \approx 18$ eV [Figs. 2(b), 2(c)] is more than 3 times lower than the literature suggests [17], and increases during electron exposure. (iii) Changes in g_0 and E_1 during exposure result in charging instabilities with a sudden change in the sign of V when E_1 becomes greater than E_0. A cusp catastrophe in Eqs. (5) is responsible for these instabilities. (iv) Electrons with $E_{land} \approx 0$ eV expose PMMA [Fig. 2(b)]; g_0 increases at roughly the same rate for $E_{land} \approx 0$ eV, as for 15–35 eV. Dissociative electron attachment likely plays an important role in determining line edge roughness (LER), proximity effects, dose efficiency, and other effects in EUV and electron lithography. (v) At field strengths >7.5 MV/cm (20 nm PMMA) dielectric breakdown gives rise to a rapid increase in g_0 and E_1 during the first few seconds of exposure.

While these results are for PMMA, experiments on exploratory EUV resists containing Sn(oxo) cages [26,27] display the same effects: sensitivity for near-zero eV electrons and strong charging instabilities. As the same basic mechanisms apply, the experimental and theoretical methodology developed here will make it possible to study such EUV resists more fully, and to contribute directly to their characterization and optimization. Surface charging, resist conductance, secondary electron emission, charging instabilities, and dielectric breakdown are not routinely considered in simulations of resist exposure, nor is the role of low electron energy processes such as dissociative electron attachment [28,29]. We suggest that these effects can no longer be ignored. During spatially patterned illumination charging will also vary spatially and electric fields will develop both normal and parallel to the surface. This will have additional ramifications for pattern definition and LER in lithography applications.

With excellent low energy beam control and built-in spectroscopic capabilities, LEEM offers a powerful new approach for studying and understanding the interactions of low energy electrons with organic materials. The ability to observe the electron energy loss spectrum during irradiation gives real-time access not only to charging phenomena, but also to changes in secondary electron emission, inelastic energy losses [30], and even electronic band structure [31,32]. Future studies of resist materials, as well as other organic and inorganic films, including biological materials such as DNA, organic semiconductors and metals, will greatly expand and enrich our understanding of the interaction of low energy electrons with soft matter of all kinds.

[1] *EUV Lithography* edited by V. Bakshi (SPIE and John Wiley & Sons, New York, 2009), ISBN 9780819469649/9780470471555.

[2] Ernst Bauer, *Surface Microscopy with Low Energy Electrons* (Springer, New York, 2014), ISBN 978-1-4939-0934-6.

[3] R. M. Tromp, M. Mankos, M. C. Reuter, A. W. Ellis, and M. Copel, Surf. Rev. Lett. **05**, 1189 (1998).

[4] A. Thete, D. Geelen, S. Wuister, S. J. van der Molen, and R. M. Tromp, Proc. SPIE 9422, Extreme EUV Lithography **94229A–94220A-5**, (2015); S. M. Schramm, J. Kautz, A. Berghaus, O. Schaff, R. M. Tromp, and S. J. van der Molen, IBM J. Res. Dev. **55**, 1:1 (2011).

[5] O. Wollersheim, H. Zumaqué, J. Hormes, D. Kadereit, J. langen, L. Häußling, P. Hoessel, and G. Hoffmann, Nucl. Instrum. Methods Phys. Res., Sect. B **97**, 273 (1995).

[6] H. Hiraoko, IBM J. Res. Dev. **21**, 121 (1977).

[7] E. M. Lehockey and I. Reid, J. Vac. Sci. Technol. A **6**, 2221 (1988).

[8] B. W. Yates and D. M. Shinozaki, J. Polym. Sci., Part B: Polym. Phys. **31**, 1779 (1993).

[9] *The Radiation Chemistry of Macromolecules Volumes I and II*, edited by M. Dole (Academic Press, New York, 1972).

[10] S. Rangan, R. A. Bartynski, A. Narasimhan, and R. L. Brainard, J. Appl. Phys. **122**, 025305 (2017).

[11] R. Gilmore, *Catastrophe Theory for Scientists and Engineers* (John Wiley & Sons, New York, 1981), ISBN 0-471-05064-4.

[12] M. Braun, F. Gruber, M.-W. Ruf, S. V. K. Kumar, E. Illenberger, and H. Hotop, Chem. Phys. **329**, 148 (2006).

[13] R. M. Tromp, Y. Fujikawa, J. B. Hannon, A. W. Ellis, A. Berghaus, and O. Schaff, J. Phys. Condens. Matter **21**, 314007 (2009).

[14] N. F. Mott and R. W. Gurney, *Electronic Processes in Ionic Crystal*, 1st ed. (Oxford University Press, Oxford, 1940); See also: M. Pope and C. E. Swenberg, *Electronic Processes in Organic Crystals and Polymer*, 2nd ed. (Oxford University Press, Oxford, 1999).

[15] D. C. Joy, M. S. Prasad, and H. M. Meyer III, J. Microsc. **215**, 77 (2004).

[16] J. Cazaux, Nucl. Instrum. Methods Phys. Res., Sect. B **244**, 307 (2006).

[17] E. A. Burke, IEEE Trans. Nucl. Sci. **NS-27**, 1760 (1980).

[18] J. J. Scholtz, D. Dijkkamp, and R. W. A. Schmitz, Philips J. Res. **50**, 375 (1996).

[19] Y. Lin and D. C. Joy, Surf. Interface Anal. **37**, 895 (2005).

[20] K. Said, G. Damamme, A. SI Ahmed, G. Moya, and A. Kallel, Appl. Surf. Sci. **297**, 45(2014).

[21] J. P. Ganachaud and A. Mokrani, Surf. Sci. **334**, 329 (1995).

[22] M. Dapor, M. Ciappa, and W. Fichtner, J. Micro/ Nanolithogr. MEMS MOEMS **9**, 023001 (2010).

[23] A. Dunaevsky, Y. Raitses, and N. J. Fisch, Phys. Plasmas **10**, 2574 (2003), and references therein.

[24] See Supplemental Material at http://link.aps.org/ supplemental/10.1103/PhysRevLett.119.266803 for more detailed information on (i) Secondary Electron Emission, (ii) The insensitivity of the result to the value of α in Eq. (4),

(iii) Various solutions to Eq. (5b), (iv) The cusp catastrophe contained in Eq. (5b), and (v) Experimental details, including native oxide, and current measurements.

[25] C. Neusel and G. A. Schneider, J. Mech. Phys. Solids **63**, 201 (2014).

[26] B. Cardineau, R. Del Re, H. Al-Mashat, M. Marnell, M. Vockenhuber, Y. Ekinci, C. Sarma, M. Neisser, D. A. Freedman, and R. L. Brainard, Proc. SPIE 9051, Advances in Patterning Materials and Processes **XXXI**, 90511B (2014).

[27] A. Thete, D. Geelen, Y. Zhang, J. Haitjema, F. Brouwer, S. J. van der Molen, and R. M. Tromp (to be published).

[28] L. Wisehart, A. Narasimhan, S. Grzeskowiak, M. Neisser, L. E. Ecola, G. Denbeaux, and R. L. Brainard, Proc. SPIE 9776, Extreme Ultraviolet (EUV) Lithography **VII**, 97762O (2016).

[29] A. Narasimhan, S. Grzeskowiak, B. Srivats, H. Herbol, L. Wisehart, C. Kelly, W. Early, L. E. Ocola, M. Neisser, G. Denbeaux, and R. L. Brainard, Proc. SPIE 9422, Extreme Ultraviolet (EUV) Lithography **VI**, 942208 (2015).

[30] Y. Fujikawa, T. Sakurai, and R. M. Tromp, Phys. Rev. Lett. **100**, 126803 (2008).

[31] H. Hibino, H. Kageshima, F.-Z. Guo, F. Maeda, M. Kotsugi, and Y. Watanabe, Appl. Surf. Sci. **254**, 7596 (2008).

[32] J. Jobst, J. Kautz, D. Geelen, R. M. Tromp, and S. J. van der Molen, Nat. Commun. **6**, 8926 (2015).